α and 2p2n emission in fast neutron-induced reactions on ^{60}Ni

N. Fotiades, M. Devlin, R. C. Haight, R. O. Nelson, S. Kunieda, and T. Kawano

Phys. Rev. C **91**, 064614 — Published 19 June 2015

DOI: 10.1103/PhysRevC.91.064614

α and $2p2n$ emission in fast neutron-induced reactions on ^{60}Ni

N. Fotiades,* M. Devlin, R. C. Haight, R. O. Nelson, S. Kunieda,† and T. Kawano

Los Alamos National Laboratory, Los Alamos, New Mexico 87545, USA

(Dated: May 18, 2015)

Abstract

Background: The cross sections for populating the residual nucleus in the reaction ${}^{A}_{Z}\mathrm{X}(n,x){}^{A-4}_{Z-2}\mathrm{Y}$ exhibit peaks as a function of incident neutron energy corresponding to the $(n,n'\alpha)$ reaction and, at higher energy, to the $(n,2p3n)$ reaction. The relative magnitudes of these peaks vary with the Z of the target nucleus.

Purpose: Study fast neutron-induced reactions on ^{60}Ni. Locate experimentally the nuclear charge region along the line of stability where the cross sections for α emission and for $2p2n$ emission in fast neutron-induced reactions are comparable as a further test of reaction models.

Methods: Data were taken using the GEANIE Ge-detector array. The broad-spectrum pulsed neutron beam of the Los Alamos Neutron Science Center's (LANSCE) WNR facility provided neutrons in the energy range from 1 to 250 MeV. The time-of-flight technique was used to determine the incident-neutron energies.

Results: Absolute partial cross sections for production of seven discrete Fe γ rays populated in $^{60}\mathrm{Ni}(n,\alpha/2pxn\gamma)$ reactions with $2 \leq x \leq 5$ were measured for neutron energies 1 MeV$<E_n<$250 MeV. Hauser-Feshbach plus pre-equilibrium theoretical calculations are compared to the experimental results.

Conclusions: There is good agreement between experimental results and theoretical predictions at lower neutron energies while discrepancies appear at higher neutron energies. The cross section for producing an isotope in fast neutron-induced reactions on stable targets via α emission at the peak of the (n,α) and $(n,n'\alpha)$ reactions is comparable to that for $2p2n$ and $2p3n$ emission at higher incident energies in the nuclear charge region around Fe.

*fotia@lanl.gov

†Present address: Nuclear Data Center, Japan Atomic Energy Agency, Tokai-mura Naka-gun, Ibaraki 319-1195, Japan

I. INTRODUCTION

There is growing interest from both basic and applied nuclear physics for studies of fast neutron-induced reactions especially at higher incident energies. In basic nuclear physics, neutron-induced reactions provide a useful means to characterize reaction mechanisms and investigate nuclear structure by imposing constraints on nuclear models. Because nuclear structure effects can have a large influence on the population of various states, and because of the difficulty in predicting such effects, it is important to have data to constrain reaction models used to predict nuclear level populations. For applications, elemental transmutation can modify material properties. Population of excited states leads directly to γ-ray heating.

From the great variety of nuclear species the α particle is one of the few clusters that play a special role. Indeed, α emission is the most common form of cluster emission in nuclear reactions because of the extremely high binding energy and relatively small mass of the α particle. At higher energies, transmutation reactions that lead to the same isotope can include also lighter particles that sum to the baryon number and charge of the alpha particle, such as $2p + 2n$, $p + d + n$, n+^{3}He, p+^{3}H, and $d + d$. Calculations indicate that for incident neutron energies well above threshold, the $2p + 2n$ probability is the largest of these and therefore we will refer to the γ rays we see as being from, for example, "$(n, n'\alpha)$" and "$(n, 2p3n)$" reactions where the residual nucleus is 4 mass units and 2 charge units less than that of the target nucleus.

Recently, population of the same nucleus in fast neutron-induced reactions via emission of an α particle at lower neutron energies and via $2p2n$ emission at higher neutron energies was observed in neutron-induced reactions on stable ^{48}Ti [1]. Earlier, strong population of isotopes via similar channels that include the $2p2n$ emission was observed in fast neutron-induced reactions on stable ^{92}Mo [2]. In both cases good agreement was found with predictions from the same reaction model for the lowest $2^+ \rightarrow 0^+$ transition. On the other hand, in fast neutron-induced reactions on a nucleus with much smaller Z it is the population via α emission that is larger, as was observed in Ref. [3] in reactions on ^{16}O.

These γ-ray measurements can be interpreted as the total production cross sections for the residual even-even nuclei since the lowest $2^+ \rightarrow 0^+$ transitions are known to be about 90% of the reaction cross section to the nucleus [4–6]. The total production cross sections are somewhat similar to those reported for proton reactions where the cross sections for product

nuclei are determined by activation [7–9]. Both approaches are relevant for testing reaction models (see, for instance, Ref. [10]). Comparisons of some data and of the complementary strengths of these approaches are discussed in section IV.

Finally, the different transitions in the residual nuclei are influenced by the angular momentum of the states and therefore are further tests of reaction models. Although calculations for the lowest $2^+ \rightarrow 0^+$ transitions in the previous studies on ^{48}Ti [1] and ^{92}Mo [2] agreed well with the measured data, those for higher-spin transitions were not uniformly successful. Thus more data for nuclei in this range of medium-weight nuclei are required for a better understanding of the physical processes modeled in the calculations.

II. EXPERIMENT

Discrete γ-ray yields were measured for Fe isotopes populated in $^{60}Ni(n, \alpha x n \gamma)$ and $^{60}Ni(n, 2p2nxn\gamma)$ reactions with $x = 0 - 3$, as a function of incident-neutron energy using the Ge γ-ray spectrometer GEANIE [11] and neutrons from the "white" source neutron beam at the LANSCE/WNR facility [12, 13]. GEANIE is located 20.34 m from the WNR spallation neutron source on the 60R (60°-Right) flight path. During the experiment GEANIE was comprised of 10 Compton-suppressed planar Ge detectors (Low Energy Photon Spectrometers - LEPS) and 10 Compton-suppressed coaxial Ge detectors. A schematic diagram of the experimental setup can be found in Ref. [14].

Source neutrons are produced in a ^{nat}W spallation target driven by an 800 MeV proton beam with an average current of $\sim 2\mu A$. The beam time structure was as follows: 40 Hz of "macropulses", $625\mu s$ long, each macropulse containing approximately 340 "micropulses", spaced every $1.8\mu s$. At this "micropulse" spacing, wrap-around problems (time overlap of high-energy neutrons of one pulse with lower-energy neutrons of the previous pulse) start at $E_n \sim 0.6$ MeV. Because the thresholds of the reactions studied here are at much higher energies, no wrap-around corrections were necessary in the analysis of the data. The energy of the neutrons was determined using the time-of-flight technique. The neutron flux on target was measured with a fission chamber, consisting of ^{235}U and ^{238}U foils [15], located 18.48 m from the center of the spallation target.

The target consisted of one $2.5cm$ square foil, $1mm$ thick, of $5.7g$ of 99.6% enriched ^{60}Ni. During three days of the experiment a natural Fe $5cm$ square foil, $0.05mm$ thick, was placed

in front of the ^{60}Ni foil. All foils were oriented normal to the neutron beam. The Ni and Fe foils were larger than the beam spot which was circular with a diameter of $\sim 2cm$. The Fe foil is included so that the known cross section at $E_n = 14.5$ MeV [16] of the strong 846.8-keV, $2^+ \rightarrow 0^+$ transition of ^{56}Fe, produced in natural Fe from inelastic scattering, would be used to normalize the cross sections obtained in the present experiment. However, ^{56}Fe was also produced in the ^{60}Ni$(n, n'\alpha)$ and ^{60}Ni$(n, 2p3n)$ reaction channels, rendering a normalization at $E_n = 14.5$ MeV complicated in the present experiment. Instead a normalization at $E_n = 5$ MeV was attempted, since this neutron energy lies below the thresholds of the $(n, n'\alpha)$ and $(n, 2p3n)$ reaction channels. The cross section for the $2^+ \rightarrow 0^+$ transition of ^{56}Fe is known also at $E_n = 5$ MeV, however, not as well as at $E_n = 14.5$ MeV, and this uncertainty introduced an additional systematic error in the cross sections obtained in the present work.

Two-parameter data were acquired for each detector consisting of time-of-flight relative to a fast proton-beam-pickoff signal and γ-ray pulse height from the Ge detectors. The data acquisition electronics consisted of a constant fraction discriminator, gating, and a TDC for the neutron-TOF measurement, and a spectroscopy amplifier and ADC for γ-ray pulse height acquisition. Escape suppression was implemented by vetoing the associated Ge signals with the corresponding BGO signals in hardware. The time-resolution of the Ge detectors is the dominant factor that determines the incident neutron energy resolution. The time resolution varies as a function of incident γ-ray energy, and ranged from 10 to 20 ns (FWHM) for the coaxial Ge detectors. This corresponds to a resolution of 0.6 to 0.9 MeV at 10 MeV incident neutron energy and 12 to 24 MeV at 100 MeV. We determine time resolutions from the FWHM of the γ-flash peak calculated for the GEANIE flight path. The γ-flash-peak time-FWHM was measured to be lowest (5 ns) for planar detectors and high-energy γ-rays ($E_\gamma \sim 1\ MeV$), while it is highest (20 ns) for coaxial detectors and low-energy γ-rays ($E_\gamma \sim 100\ keV$).

Relative detector efficiencies were determined using a ^{152}Eu calibrated γ-ray source. Corrections for the finite beam spot size, γ-ray attenuation in the samples (both Ni and Fe), and the contribution from neutrons produced by scattering and reactions in the targets (secondary effects), were modeled for the present experiment using the MCNP Monte-Carlo radiation transport code [17]. Electronic "dead-times" were measured using scalers and corrections were applied to the data. During the experiment the data were stored on a disk

system using the MIDAS data acquisition system [18]. A total of $\sim 3.4 \times 10^7$ γ singles and higher fold data were recorded in five coaxial detectors that were selected for the best energy and time resolution. The five coaxial detectors used in the analysis were at angles -25^o, -77^o, 78.5^o, and 102^o with respect to the neutron beam. The effect of angular distributions of the γ rays is expected to be less than 1% for incident-neutron energies a few MeV above each reaction-channel threshold (see, for instance, Ref. [19], and references therein) and it was not included in the present analysis.

III. EXPERIMENTAL RESULTS

The cross sections for emission of a total of seven γ-rays of ^{54,55,56,57}Fe [20–23] were determined. The observed γ-rays are included in the level schemes in Fig. 1. Plots of the obtained cross sections versus incident-neutron energy for the 1222.5- and 1238.3-keV transitions of ^{55,56}Fe were previously reported in the proceedings of a conference in Ref. [24]. The cross sections as a function of incident-neutron energy, deduced from the present work for all transitions in Fig. 1, are given in Tables I-VII. All cross-section errors reported in Tables I-VII are statistical. Estimated total systematic uncertainties of 10-12% (depending on E_γ and E_n) are additional with contributions from the detection efficiency of 1.5-4.0% (varies with E_γ) and from the neutron flux of 1.0-2.5% (varies with E_n), as well as contributions from the normalization process (8%), the target thickness (6%) and the "dead-time" corrections (3%) that do not depend on E_γ and E_n. Uncertainties in the fission foil thickness, fission cross section, ionization chamber efficiency, and MCNPX simulations are also included. The 8% contribution from the normalization process is deemed the principal contribution in the overall uncertainty. The obtained cross sections for the $2_1^+ \rightarrow 0_1^+$ transitions in the residual nuclei ^{54}Fe and ^{56}Fe represent a large part of the total cross section of the corresponding reaction channels, since almost all decaying γ cascades proceed through these transitions as has been noted previously at lower reaction energies [4–6]. In the odd-mass isotopes of ^{55,57}Fe, the γ-ray cascades to the ground state proceed through different paths via several low-lying levels, hence, the obtained cross sections for the transitions feeding the lowest $\frac{3}{2}^-$ levels of ^{55,57}Fe in Fig. 1 represent only a part of the total cross section of the corresponding reaction channels. However, no other previously-known transition of ^{55,57}Fe was observed in the present experiment suggesting that all feeding of the ground states in ^{55,57}Fe that by-

passes the observed γ rays lies below the detection limits of the present experiment. Thus, for the residual isotopes $^{54-57}$Fe, the γ-ray production data give a good estimate of the total production cross section.

During the off-line analysis a matrix (two-dimensional array) of γ-ray energy (E_γ) versus time-of-flight (TOF) was built. By gating on the time-of-flight axis in this matrix, γ-ray spectra in certain neutron energy bins were obtained. The widths of the adopted neutron-energy bins in Tables I-VII can be deduced by $2 \times \Delta E_n$ while the mean energy of each bin is quoted as the incident neutron energy E_n. For the 122.1 keV γ ray of ^{57}Fe in Table I wider neutron energy bins (20 ns) were used compared to the rest of the γ rays (15-ns bins) in order to account for the worse time resolution of the coaxial detectors at such low energies. The fitting of the peaks in the γ-ray spectra with a gaussian line shape gives the yield of a γ ray at a certain neutron-energy bin. In some cases the peaks observed in our spectra originated from more than one transition. This was the case for the 1222.5-keV transition of ^{55}Fe [21] and the 1224.0-keV, $\frac{9}{2}^- \rightarrow \frac{7}{2}^-$ transition of ^{57}Co [23], the $(n, p3n)$ reaction channel, where deconvolution of the peak and, hence, of the cross sections for the two transitions, was not possible. Hence, the cross section given in Table III is the summed cross section for production of both transitions.

IV. DISCUSSION

In Fig. 2 the cross sections obtained for the three observed transitions of ^{56}Fe and one transition of ^{55}Fe are plotted. The shapes of the excitation functions for the observed transitions of ^{56}Fe are very similar. Two well-separated peaks are present in all cases, the one at lower neutron energies originating from emission that includes an α particle while the one at higher neutron energies includes $2p2n$ emission and, of course, all other possible sizable reaction paths that are open at higher energies and can not be distinguished experimentally. Indeed, a calculation at various neutron energies of all the possible reaction paths and their production cross section using the code CoH_3 [25] predicts that the $2p3n$ path has the largest component in the production of ^{56}Fe at $E_n = 75$ MeV, however, the $p2nd$ path is significant too (see Table VIII and Fig. 3). The same effect of a double-humped structure is present also in the cross sections obtained for the one transition observed in ^{57}Fe (see Table I) and the one transition of ^{54}Fe (see Table VII). For the second transition observed in ^{55}Fe (see

Table III) this effect can not be seen because this transition is an unresolved doublet in the obtained spectra.

In Fig. 2 results of theoretical calculations for the production of the γ rays from two reaction models are included. The first model (solid lines in Fig. 2) is the CoH_3 [25] code mentioned in the previous paragraph but extended to $E_n = 120$ MeV. The other model (dashed lines in Fig. 2) extends up to much higher incident-neutron energies ($E_n = 200$ MeV). The latter calculation was described in detail in a recent publication [26] and was expanded here to $E_n = 200$ MeV from 150 MeV that was reported in the previous publication. It is based on the Hauser-Feshbach code GNASH [27] with incorporation of a cluster emission model to describe the pre-equilibrium process. This code was used also in the calculations described in the previous LANSCE experiments referenced in this work [1–3]. The two nuclear reaction codes used in the present work, GNASH and CoH_3, are based on the same reaction mechanisms, but the decay of the compound nuclei is calculated differently for the multiple particle emission at high energies. The compound nuclear reaction can produce the same residual nucleus through many reaction paths. As shown in Table VIII and in Fig. 3, ^{56}Fe is produced in several different reaction paths above 30 MeV incident-neutron energy. In GNASH, the production probabilities of ^{56}Fe by these reaction paths are stored in a common array, while CoH_3 separates them. With this technique CoH_3 can split the total ^{56}Fe production cross section into the different components. However, several compound nuclei emerging at higher energies tend to exhaust the computational resources, hence, the CoH_3 calculations cannot be performed above $\sim$120 MeV incident-neutron energy.

In the calculations described in the present work low-lying transitions were explicitly entered in the calculations based on the evaluated γ-ray branching ratios, which are based on experiments. For the γ-feeding from highly excited states, the photon strength function model including E1, M1, E2, M2, and E3, was used. The M2 and E3 contributions are almost negligible. For the E1 photon strength function, the so-called generalized Lorentzian form proposed by Kopecky and Uhl [28] was used, while for the higher multipolarities, the standard Lorentzians were used. These parameters were taken from the RIPL-3 compilation [29].

There is good agreement between the GNASH theoretical predictions and the experimental results in the α reaction channels, i.e., below 50 MeV, in Fig. 2, at least for the transitions from low-spin states. However, at higher incident-neutron energies the agreement is poor.

This overestimation was also found in CoH_3 with a standard parametrization of the level densities and the pre-equilibrium parameters. Attempts were made to optimize this calculation to the GEANIE data by varying the level density parameters. However, the sensitivities of each level density parameter were never high enough to reproduce the data, since there are many reaction paths that end up with ^{56}Fe and reducing one reaction path results in flux increase in other channels. As a practical solution the reactions (n,dX), (n,tX), and (n,^{3}HeX) were suppressed in CoH_3 by reducing the single particle level densities for the deuteron, triton, and ^{3}He emission channels by 50%. A similar modification can be made by re-scaling the phenomenological parameter of 1/80 obtained by Kalbach [30]. Although this adjustment increases somewhat the $(n, 2p3n)$ channel cross section, the total ^{56}Fe production cross section becomes smaller. As a result of this suppression the predictions by CoH_3 in Fig. 2 are in better agreement at higher incident-neutron energies with the experimental results. The observed differences between theoretical predictions and experimental results can be attributed to the level density parameter used in the Hauser-Feshbach calculation and/or to the description of the pre-equilibrium process. The first light particle to be emitted at higher neutron energies is most likely a pre-equilibrium nucleon and the rest of the particles are likely emitted from the compound nucleus since the probability for multi-particle emission during the pre-equilibrium process is very small [26]. Hence, the incorporation in the calculation of a pre-equilibrium model is essential in describing the processes at higher incident-neutron energies.

In Fig. 2 the result of the GNASH calculation for the total production of ^{56}Fe is included (dotted line). The calculated cross section for the $2_1^+ \rightarrow 0_1^+$ transition represents a large part of the calculated total cross section of the ^{56}Fe reaction channel, since almost all decaying γ cascades proceed through this transition. At lower incident-neutron energies where there is good agreement between the experimental results and the theoretical predictions, the experimentally observed cross section for the $2_1^+ \rightarrow 0_1^+$ transition represents a large part of the total cross section of the reaction channel, as expected. Weak transitions that are known previously to feed the ground state of ^{56}Fe and by-pass the 2_1^+ state [22] were not observed in the present experiment.

Production of the same γ rays in the (n, α) channel at lower neutron energies and in the $(n, 2p2n)$ channel at higher neutron energies has been observed before at LANSCE with GEANIE and with pre-GEANIE Ge-detector set-ups. The present experimental results are

compared to previous experimental results in Fig. 4. In Fig. 4.a data from a pre-GEANIE experiment are shown where the α-peak is dominant in the γ-ray-production cross section of the ^{16}O(n,$\alpha/2p2n$)^{13}C reactions (data taken from figure 15 of Ref. [3]); in Fig. 4.b data from a GEANIE experiment are shown where the α peak is still larger than the $(n, 2p2n)$ peak in the ^{48}Ti(n,$\alpha/2p2n$)^{45}Ca reactions (data taken from figure 9 of Ref. [1]); data from the present work are shown in Fig. 4.c where the α peak is of comparable size to the $(n, 2p2n)$ peak in the ^{60}Ni(n,$\alpha/2p2n$)^{57}Fe reactions (data taken from Table I); and, finally, in Fig. 4.d data from a GEANIE experiment are shown where the α peak is smaller than the $(n, 2p2n)$ peak in the ^{92}Mo(n,$\alpha/2p2n$)^{89}Zr reactions (data taken from figure 11 of Ref. [2]). Thus, Fe emerges as the nuclear charge region along the stability line where the cross section for producing an isotope in fast neutron-induced reactions on stable targets via α emission at the peak of the (n, α) and $(n, n'\alpha)$ reactions is comparable to that for $2p2n$ and $2p3n$ emission at higher incident energies.

The same effect and conclusions are supported from comparison of the data in the $(n, n'\alpha)$ channel as it can be seen in Fig. 5. All transitions in Fig. 5 are the $2_1^+ \rightarrow 0_1^+$ transitions in the corresponding isotopes, hence, any possible dependence of this effect on the spin-parity of the emitting state is the same in all cases. It is also interesting to note that the thresholds for the $(n, 2p3n)$ reactions on all of these target nuclei are very similar and span the range only from 34 to 39 MeV. A more quantitative illustration of the effect is shown in Fig. 6 where the ratio of the maximum cross-section values in the $2p3n$ peak and in the αn peak is drawn versus the charge of the residual nucleus for all transitions in Fig. 5. The same values are also plotted for the GNASH and CoH_3 predictions indicating that the overall trend is reproduced by the calculations but there are still differences in the individual values.

Solid curves in Figs. 4 and 5 are the results of the CoH_3 prediction while the result of the GNASH calculation for the 122.1 keV γ ray of ^{57}Fe is also included in Fig. 4 (dashed line). The GNASH predictions for all other γ rays in Figs. 4 and 5 were given in Refs. [1–3] and in Fig. 2 for the 846.8-keV transition. The conclusions drawn earlier from Fig. 2 about the differences in the predictions of the two models are also valid in Figs. 4 and 5. For the 122.1 keV transition in Fig. 4.c the extra strength observed experimentally around $E_n = 35$ MeV compared to both theoretical predictions could be an indication of possible contamination from an unknown origin of this transition in the experimental spectra around these incident-neutron energies.

The present measurements are related to studies made of proton activation cross sections, which are also used to test reaction models. Proton activation cross sections in this range of incident nucleon energy are often investigated by the stacked foil technique (see e.g. Refs. [7, 8]) although there are also important differences that make the two approaches complementary. In our measurements, reactions that produce even-even nuclei have strong $2_1^+ \rightarrow 0_1^+$ transitions that are generally known to have a cross section that is 90% or more of the production cross section [4–6]. The calculations described in the present work show that the ratio of the lowest transition to the total production depends on the reaction and the neutron incident energy, and it tends to stay at a large fraction. For instance, at 20 MeV incident energy, in the case of the ^{60}Ni(n, n') reaction channel the production cross section for the $2_1^+ \rightarrow 0_1^+$ transition is 89% of the total inelastic scattering, while in the case of the $(n, n'\alpha)$ reaction channel, the production cross section for the 846.8 keV transition is 83% of the total channel cross section. Hence, the present data together with our previous measurements on neutron-induced reactions on ^{A}Z leading to $^{A-4}$(Z-2) can be interpreted as production cross sections as shown in Fig. 7. An example of proton-activation cross section determined by the stacked foil technique is also given on the figure, where contributions from $(p, p'\alpha)$ and $(p, 3p2n)$ reactions can be inferred. It is also worth mentioning here that for some incident neutron energies the partial cross sections obtained for the transitions in the present work can account for a large percentage of the total α reaction cross section. As it can be seen in Fig. 8, the sum of the cross sections obtained for the lowest transitions in Fig. 1 between 20- and 30-MeV incident neutron energy corresponds to a large part of the measured total α reaction cross section reported in Ref. [26].

Differences between the measurements of proton activation via stacked foils and our neutron-induced γ-ray production are many and the example of the ^{51}V$(p, x)^{47}$Sc reaction illustrates some of them. (1) The activation cross section measurements require that the residual nucleus be radioactive. This requirement eliminates most of the even-even target $\rightarrow$ even-even residual nuclei such as those produced by $(p, p'\alpha)$ reactions as the residual nuclei are often stable, such as the ^{60}Ni $\rightarrow$ ^{56}Fe case studied here. (2) Other even-even targets are eliminated because rather thick elemental samples that are mixture of isotopes are used in order to reduce the incident proton energy as the beam passes through the stack. Enriched isotope targets can be prohibitively expensive. (3) The activation cross sections are for cumulative activation as opposed to independent production. For the displayed

^{51}V$(p,x)^{47}$Sc data for example, at high energies there can be production of ^{47}Ca, which decays into ^{47}Sc with a 4.5 day half life. Although the production of ^{51}V$(p,x)^{47}$Ca cross section is probably not large, the data in Fig. 7 at the high energies have some component from this isotope after it decays to ^{47}Sc. A residual nucleus such as ^{46}Sc, which is shielded from beta decay of isobars, can remove this complication. (4) Finally, the γ-ray production data give production cross sections for many short-lived levels. Cumulative activation cross sections give the production cross sections for the ground state (if radioactive) and relatively long-lived isomers (if any). Thus prompt γ-ray production measurements yield many more production cross sections than activation cross section measurements and provide data that are sensitive to angular momentum effects in the reaction model.

V. SUMMARY

In conclusion, partial cross sections for seven transitions in the ^{60}Ni$(n,\alpha xn)^{57-x}$Fe have been measured for neutron energies 1 MeV$< E_n <$250 MeV. The Fe isotopes are also produced in the $(n,2p2nx)$ channels at higher incident-neutron energies. The experimental results are compared with results from two theoretical calculations. Good agreement between theoretical predictions and the experimental results was observed in the α reaction channels, at least for the transitions emitted by low-spin states. The experimental results indicate that in the nuclear charge region around Fe the cross section for producing an isotope in fast neutron-induced reactions on stable targets via α emission at the peak of the (n,α) and $(n,n'\alpha)$ reactions is comparable to that for $2p2n$ and $2p3n$ emission at higher incident energies.

Acknowledgments

This work was performed under the auspices of the U.S. Department of Energy (DOE) under Contract No. DE-AC52-06NA25396. This work has benefitted from use of the LANSCE accelerator facility supported under DOE Contract No. DE-AC52-06NA25396.

[1] D. Dashdorj *et al.*, Nucl. Sci. Eng. **157**, 65 (2007).

[2] P. E. Garrett *et al.*, Phys. Rev. C **62**, 054608 (2000).

[3] R. O. Nelson, M. B. Chadwick, A. Michaudon, and P. G. Young, Nucl. Sci. Eng. **138**, 105 (2001).

[4] R. B. Day, Phys. Rev. **102**, 767 (1956).

[5] J. R. Huizenga and R. Vandenbosch, Phys. Rev. **120**, 1305 (1960).

[6] R. Vandenbosch and J. R. Huizenga, Phys. Rev. **120**, 1313 (1960).

[7] G. Friedlander, J. Hudis, and R. L. Wolfgang, Phys. Rev. **99**, 263 (1955).

[8] R. Michel *et al.*, Nucl. Instr. Meth. in Phys. Res. B **129**, 153 (1997); and references therein.

[9] R. Michel, G. Brinkmann, H. Weigel and W. Herr, Nucl. Phys. **A322**, 40 (1979).

[10] P. E. Hodgson and E. Běták, Phys. Reports, **374**, 1 (2003).

[11] J. A. Becker and R. O. Nelson, Nuclear Physics News International **7**, 11 (June, 1997).

[12] P. W. Lisowski, C. D. Bowman, G. J. Russell, and S. A. Wender, Nucl. Sci. Eng. **106**, 208 (1990).

[13] P. W. Lisowski and K. F. Schoenberg, Nucl. Instr. Meth. in Phys. Res. A **562**, 910 (2006).

[14] N. Fotiades *et al.*, Phys. Rev. C **69**, 024601 (2004).

[15] S. A. Wender, S. Balestrini, A. Brown, R. C. Haight, C. M. Laymon, T. M. Lee, P. W. Lisowski, W. McCorkle, R. O. Nelson, and W. Parker, Nucl. Instr. Meth. A **336**, 226 (1993).

[16] R. O. Nelson, N. Fotiades, M. Devlin, J. A. Becker, P. E. Garrett, and W. Younes, Proceedings of the International Conference on Nuclear Data for Science and Technology, Santa Fe, New Mexico, 2004, ed. R. C. Haight, M. B. Chadwick, T. Kawano and P. Talou, AIP Conference Proceedings 769, 838 (2005)

[17] MCNPX User's Manual, Version 2.6.0, edited by D. B. Pelowitz, Los Alamos National Laboratory Controlled Publication LA-CP-07-1473 (2007)

[18] MIDAS home page, midas.psi.ch/htmldoc, accessed 2015.

[19] N. Fotiades, M. Devlin, R. O. Nelson, and T. Granier, Phys. Rev. C **87** 044336 (2013).

[20] D. Yang and J. Huo, Nucl. Data Sheets **121**, 1 (2014).

[21] J. Huo, Nucl. Data Sheets **109**, 787 (2008).

[22] J. Huo, S. Huo, and Y. Dong, Nucl. Data Sheets **112**, 1513 (2011).

[23] M. R. Bhat, Nucl. Data Sheets **85**, 415 (1998).

[24] N. Fotiades, M. Devlin, R. C. Haight, T. Kawano, S. Kunieda, and R. O. Nelson, Nucl. Data Sheets **119**, 124 (2014).

[25] T. Kawano *et al.*, J. Nucl. Sci. Technol. **47**, 462 (2010).

[26] S. Kunieda *et al.*, Phys. Rev. C **85**, 054602 (2012).

[27] P. G. Young, E. D. Arthur, and M. B. Chadwick, Proceedings of the IAEA Workshop on Nuclear Reaction Data and Nuclear Reactors - Physics, Design and Safety, Trieste, Italy, April 15 - May 17, 1996, ed. A. Gandini and G. Reffo, World Scientific Publishing, Ltd., Singapore, 227-404 (1998); and P.G. Young, E.D. Arthur and M.B. Chadwick, Los Alamos National Laboratory report No. LA-UR-96-3739 (1996).

[28] J. Kopecky and M. Uhl, Phys. Rev. C **41**, 1941 (1990).

[29] Reference Input Parameter Library (RIPL-3), International Atomic Energy Agency, Nuclear Data Services, https://www-nds.iaea.org/RIPL-3/

[30] C. Kalbach, Phys. Rev. C **71**, 034606 (2005).

TABLE I: Cross sections for the 122.1 keV, $\frac{5}{2}^- \rightarrow \frac{3}{2}^-$ transition of ^{57}Fe. The mean energy of each neutron energy bin is quoted. Each bin is $2 \times \Delta E_n$ wide.

E_n (MeV)	ΔE_n (MeV)	σ (mb)	$\Delta\sigma$ (mb)	E_n (MeV)	ΔE_n (MeV)	σ (mb)	$\Delta\sigma$ (mb)
5.0	0.2	2.0	1.1	29.3	2.3	8.2	1.1
5.3	0.2	3.6	1.1	34.3	2.9	11.5	1.1
5.7	0.2	4.5	1.1	40.8	3.8	14.2	1.1
6.1	0.2	3.1	1.1	49.3	5.1	15.8	1.1
6.5	0.2	6.0	1.1	61.0	6.9	12.1	0.9
7.0	0.3	8.5	1.1	74.9	9.0	8.9	1.0
7.5	0.3	6.1	1.2	98.0	14.1	7.3	0.9
8.1	0.3	9.7	1.2	134.8	23.0	4.7	0.8
8.8	0.4	8.0	1.2	200.1	42.3	1.1	0.8
9.6	0.4	8.1	1.3				
10.4	0.5	12.6	1.3				
11.4	0.5	13.2	1.4				
12.6	0.6	12.5	1.4				
13.9	0.7	12.5	1.4				
15.4	0.9	8.5	1.4				
17.3	1.0	4.2	1.3				
19.5	1.2	6.6	1.3				
22.1	1.5	3.0	1.2				
25.3	1.8	5.3	1.2				

TABLE II: Cross sections for the 846.8 keV, $2^+ \rightarrow 0^+$ transition of ^{56}Fe. The mean energy of each neutron energy bin is quoted. Each bin is $2 \times \Delta E_n$ wide.

E_n (MeV)	ΔE_n (MeV)	σ (mb)	$\Delta\sigma$ (mb)
12.1	0.4	8.5	4.9
13.0	0.5	8.4	4.9
14.0	0.6	16.9	4.6
15.2	0.6	17.4	4.6
16.5	0.7	21.3	4.6
18.0	0.8	43.5	5.7
19.7	0.9	52.4	5.8
21.6	1.1	67.3	5.7
23.9	1.3	83.4	5.6
26.5	1.5	86.5	5.3
29.6	1.7	72.6	4.9
33.3	2.1	55.8	4.4
37.8	2.5	34.4	3.9
43.3	3.1	29.5	3.3
50.0	3.9	29.6	3.1
58.6	5.0	54.7	3.6
69.3	6.0	77.2	3.5
84.4	9.4	78.0	2.8
105.0	13.4	66.8	2.5
134.4	19.5	62.4	2.3
176.8	29.6	52.3	2.1
238.8	47.3	48.1	2.5

TABLE III: Cross sections for the 1222.5 keV, $\frac{11}{2}^- \rightarrow \frac{7}{2}^-$ transition of ^{55}Fe and the 1224.0 keV, $\frac{9}{2}^- \rightarrow \frac{7}{2}^-$ transition of ^{57}Co. The mean energy of each neutron energy bin is quoted. Each bin is $2 \times \Delta E_n$ wide.

E_n (MeV)	ΔE_n (MeV)	σ (mb)	$\Delta\sigma$ (mb)
29.6	1.7	8.8	3.6
33.3	2.1	11.6	3.9
37.8	2.5	15.5	3.6
43.3	3.1	33.2	3.9
50.0	3.9	55.0	4.3
58.5	5.3	64.1	3.6
69.6	7.0	45.1	3.1
84.4	9.4	43.0	2.8
105.0	13.4	36.3	2.6
134.4	19.5	34.4	2.3
176.8	29.6	30.4	2.2
238.8	47.3	24.3	2.6

TABLE IV: Cross sections for the 1238.3 keV, $4^+ \rightarrow 2^+$ transition of ^{56}Fe. The mean energy of each neutron energy bin is quoted. Each bin is $2 \times \Delta E_n$ wide.

E_n (MeV)	ΔE_n (MeV)	σ (mb)	$\Delta\sigma$ (mb)
12.1	0.4	0.4	4.2
13.0	0.5	6.2	4.4
16.5	0.7	5.3	3.5
18.0	0.8	19.6	4.8
19.7	0.9	23.4	4.6
21.6	1.1	37.8	5.0
23.9	1.3	48.1	5.0
26.5	1.5	62.9	4.9
29.6	1.7	49.2	4.2
33.3	2.1	41.1	3.9
37.8	2.5	31.1	3.6
43.3	3.1	22.2	3.3
50.0	3.9	18.8	2.9
58.6	5.0	39.3	3.3
69.3	6.0	50.2	3.0
84.4	9.4	56.0	3.0
105.0	13.4	46.2	2.7
134.4	19.5	41.7	2.4
176.8	29.6	38.3	2.3
238.8	47.3	40.9	2.8

TABLE V: Cross sections for the 1303.4 keV, $6^+ \rightarrow 4^+$ transition of ^{56}Fe. The mean energy of each neutron energy bin is quoted. Each bin is $2 \times \Delta E_n$ wide.

E_n (MeV)	ΔE_n (MeV)	σ (mb)	$\Delta\sigma$ (mb)
16.5	0.7	2.4	3.5
21.6	1.1	7.8	3.4
23.9	1.3	14.2	3.8
26.5	1.5	13.8	3.6
29.6	1.7	11.4	3.2
33.3	2.1	17.2	3.5
37.8	2.5	7.4	3.1
43.3	3.1	0.9	2.3
58.5	5.3	9.7	2.2
69.6	7.0	16.5	2.3
84.4	9.4	22.7	2.2
105.0	13.4	13.8	1.9
134.4	19.5	12.1	1.7
176.8	29.6	10.5	1.6
238.8	47.3	9.9	2.0

TABLE VI: Cross sections for the 1316.4 keV, $\frac{7}{2}^- \rightarrow \frac{3}{2}^-$ transition of ^{55}Fe. The mean energy of each neutron energy bin is quoted. Each bin is $2 \times \Delta E_n$ wide.

E_n (MeV)	ΔE_n (MeV)	σ (mb)	$\Delta\sigma$ (mb)
29.6	1.7	2.3	2.9
33.3	2.1	7.0	2.9
37.8	2.5	14.4	3.1
43.3	3.1	16.4	2.7
50.0	3.9	12.1	3.0
58.6	5.0	10.5	2.6
69.3	6.0	14.4	2.1
84.4	9.4	16.1	2.0
105.0	13.4	19.2	1.9
134.4	19.5	19.4	1.8
176.8	29.6	17.5	1.7
238.8	47.3	15.6	2.0

TABLE VII: Cross sections for the 1408.1 keV, $2^+ \rightarrow 0^+$ transition of ^{54}Fe. The mean energy of each neutron energy bin is quoted. Each bin is $2 \times \Delta E_n$ wide.

E_n (MeV)	ΔE_n (MeV)	σ (mb)	$\Delta\sigma$ (mb)
43.3	3.1	5.8	2.5
50.0	3.9	13.0	2.4
58.6	5.0	17.8	2.8
69.3	6.0	13.2	2.2
84.4	9.4	15.0	2.1
105.0	13.4	19.2	2.0
134.4	19.5	18.8	1.8
176.8	29.6	20.5	1.8
238.8	47.3	19.7	2.2

TABLE VIII: Reaction Q-values and predicted cross sections at $E_n = 25, 50, 75$ MeV of all possible reaction paths producing ^{56}Fe in neutron-induced reactions on ^{60}Ni using the code CoH_3 [25]. The cross section values are also plotted in Fig. 3.

Q-value	Particles emitted						σ (mb)		
(MeV)	n	p	α	d	t	^3He	$E_n = 25$MeV	$E_n = 50$MeV	$E_n = 75$MeV
-6.29	1		1				104.29	24.675	7.883
-23.88				1	1		0.0	0.0348	0.026
-26.11	1	1			1		0.0	2.2544	1.743
-26.87	2					1	0.0	0.7428	0.805
-30.14	1			2			0.0	0.0567	0.229
-32.36	2	1		1			0.0	2.9244	14.812
-34.59	3	2					0.0	7.8580	98.698

FIG. 1: Level schemes showing the transitions of Fe isotopes observed in the present work. All γ-ray and level energies are in keV. Data taken from Refs. [20–23].

FIG. 2: Cross sections for the three transitions of ^{56}Fe and a transition feeding directly the ground state of ^{55}Fe in Fig. 1. The x parameter indicates the various reaction channels. Results from the theoretical calculations from CoH_3 (solid lines) and from GNASH (dashed lines) are included for the production of these γ rays. The GNASH prediction for the total production of ^{56}Fe (dotted line) is also included in the upper figure.

FIG. 3: Predicted cross sections of all possible reaction paths producing ^{56}Fe in neutron-induced reactions on ^{60}Ni using the code CoH_3 [25]. Each path is labelled with the emitted particles that it includes. The total (sum of all possible reaction paths) cross section for production of ^{56}Fe is also plotted and labelled as "Total". The plotted values at neutron energies 25, 50, and 75 MeV are also given in Table VIII.

FIG. 4: Cross sections for transitions of ^{13}C, ^{45}Ca, ^{57}Fe, and ^{89}Zr populated in the (n,α) reaction at lower neutron energies and in the $(n,2p2n)$ reaction at higher neutron energies: (a) data taken from Ref. [3], (b) data taken from Ref. [1], (c) data from present work (see Table I), and (d) data taken from Ref. [2]. The solid lines are the results for the production of these γ rays from the CoH_3 calculation. The dashed line is the result for the production of the 122.1 keV γ ray from the GNASH calculation.

FIG. 5: Cross sections for transitions of ^{12}C, ^{44}Ca, ^{56}Fe, and ^{88}Zr populated in the $(n,n'\alpha)$ reaction at lower neutron energies and in the $(n,2p3n)$ reaction at higher neutron energies: (a) data taken from Ref. [3], (b) data taken from Ref. [1], (c) data from present work (see Table II), and (d) data taken from Ref. [2]. The solid lines are the results for the production of these γ rays from the CoH_3 calculation.

FIG. 6: Ratio of maximum cross-section values for the transitions in Fig. 5 (circles). The ratio between the $2p3n$ peak and αn peak is plotted versus the nuclear charge of the residual nucleus in the corresponding reactions. The same values but for the GNASH and CoH_3 predictions are plotted in triangles and diamonds, respectively. Data taken from Refs. [1–3] and the present work.

FIG. 7: Experimental data from Fig. 5 (from Refs. [1–3] and the present work) compared to data on $^{51}V(p,x)^{47}Sc$ measured by the stacked foil technique (from Refs. [8, 9]). Lines are to guide the viewer's eye.

FIG. 8: Experimental data for the total $^{60}Ni(n,x\alpha)$ cross section from Fig. 7(b) of Ref. [26] (circles) compared to the partial cross section (squares) obtained by summing the cross sections for the four lowest transitions (122.1-, 846.8-, 1316.4-, and 1408.1-keV) in Fig. 1 using 15-ns time-of-flight bins for all transitions.

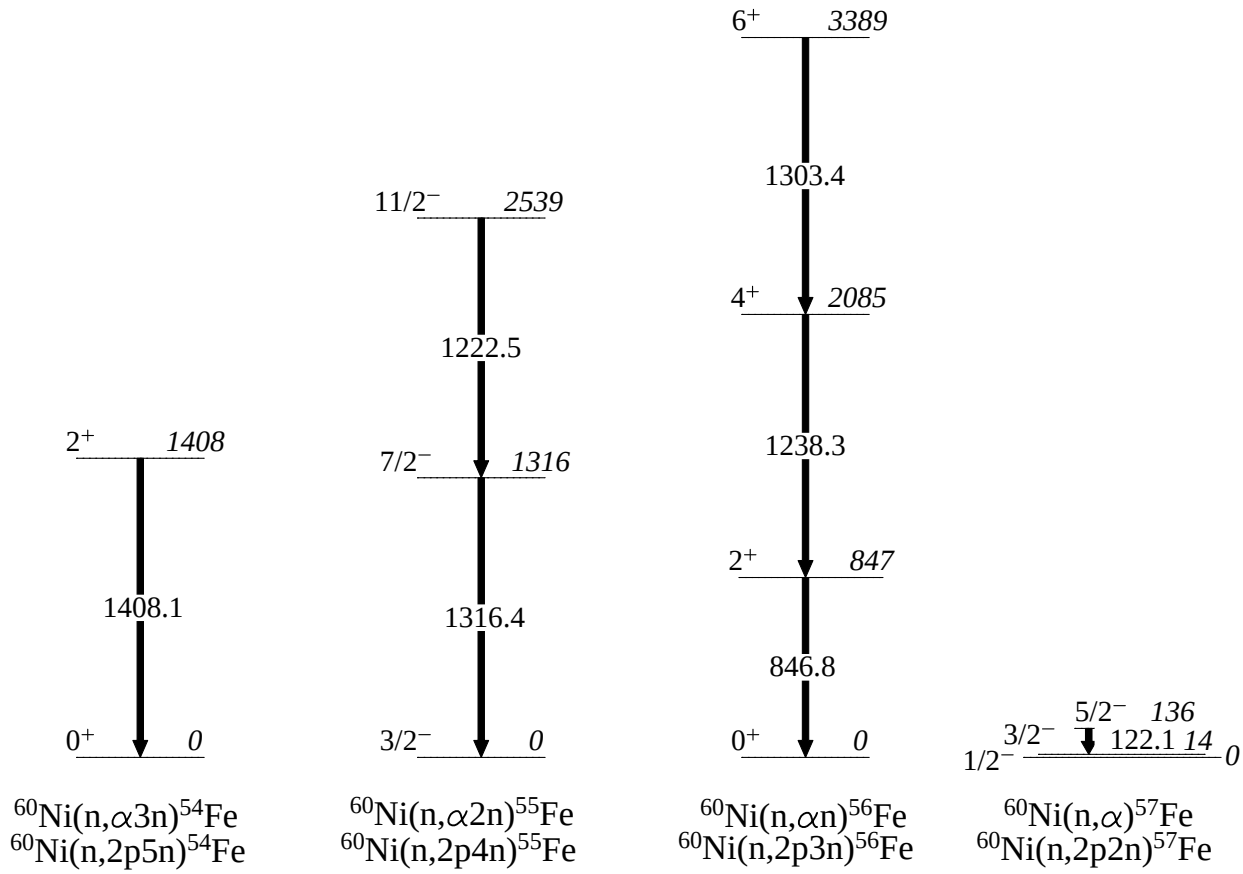

Figure 1 18May2015

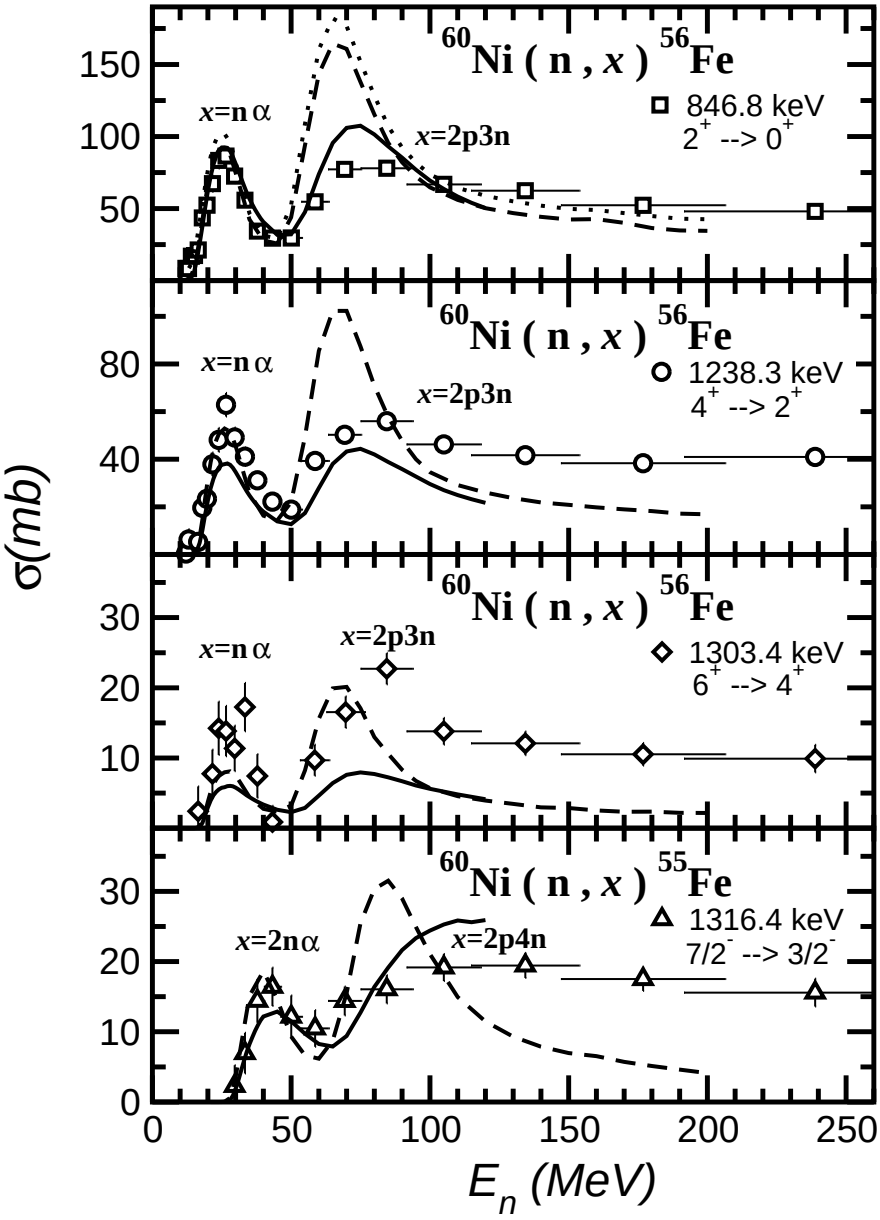

Figure 2 18May2015

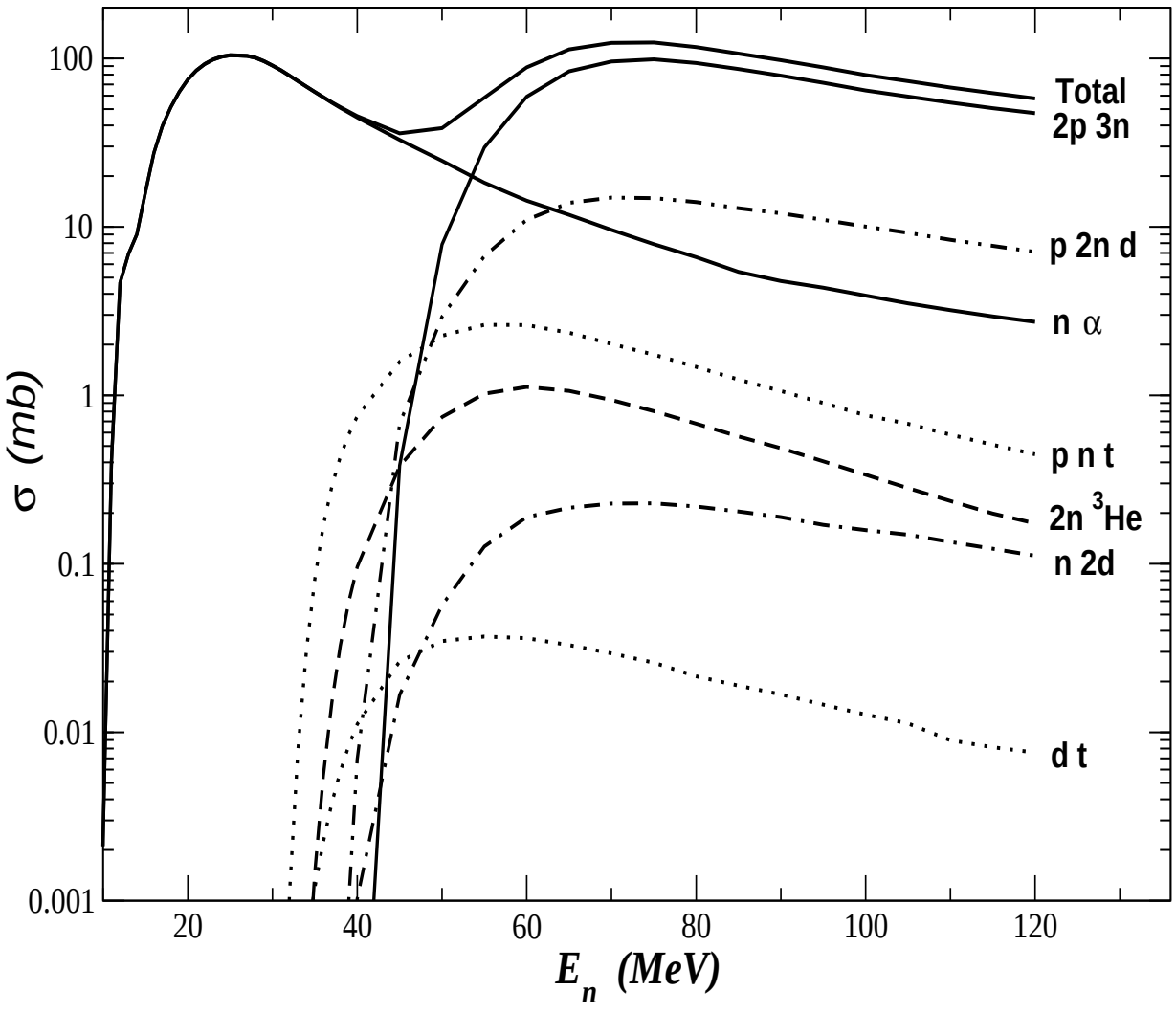

Figure 3 18May2015

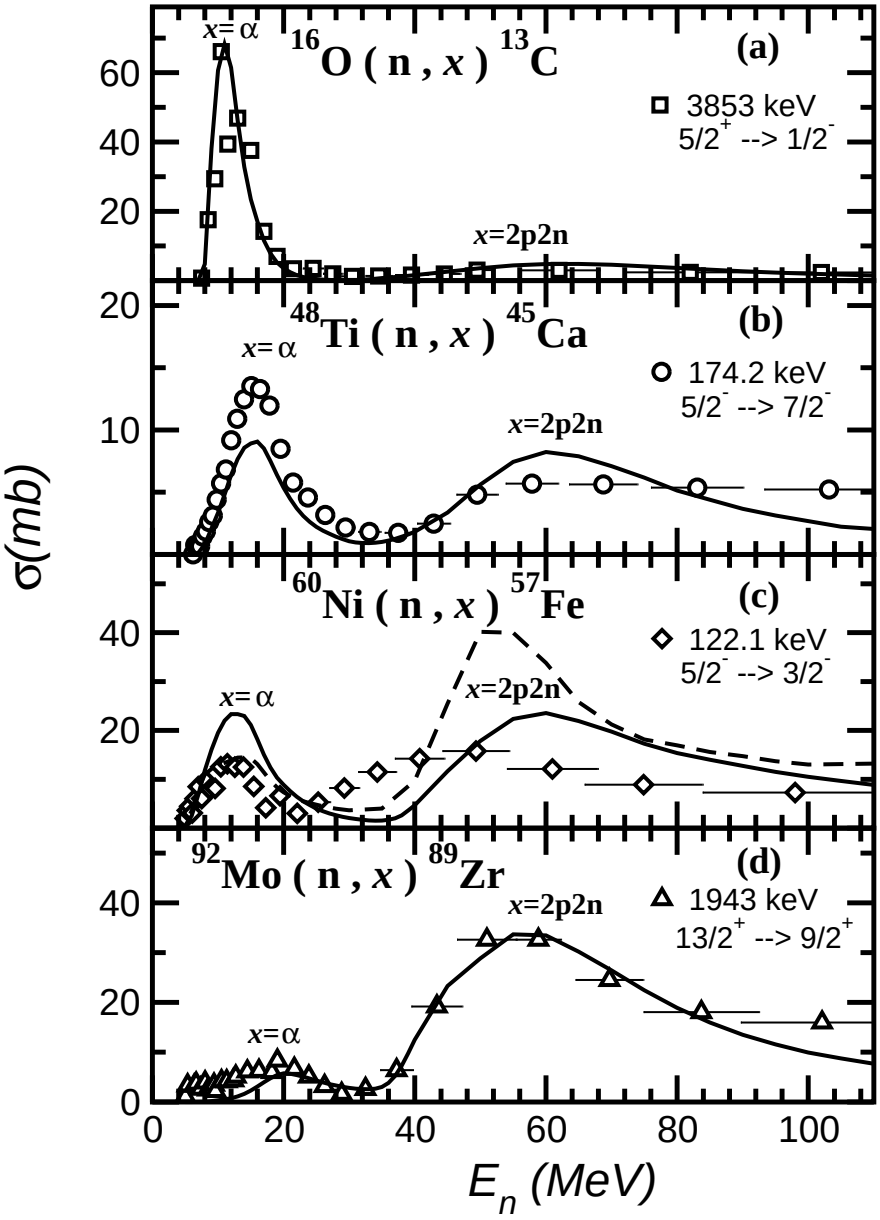

Figure 4 18May2015

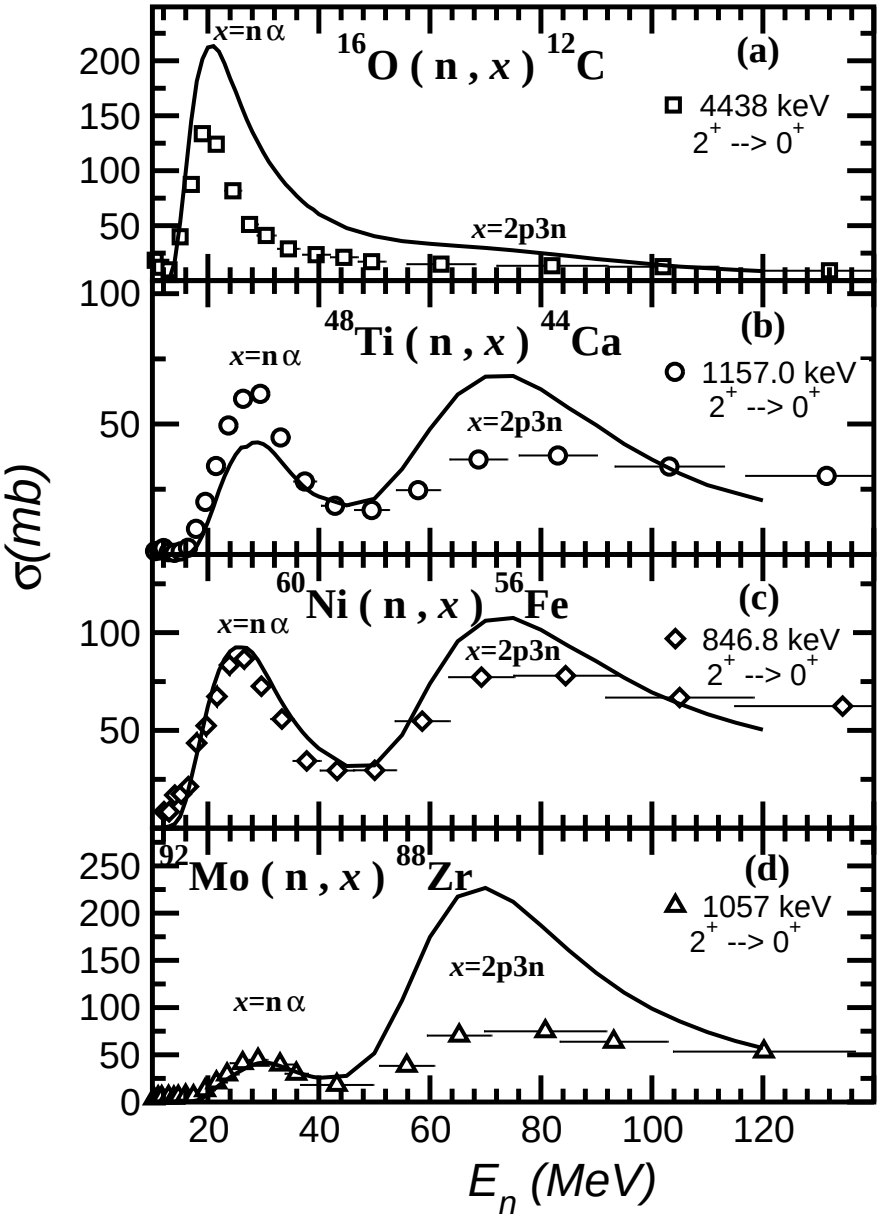

Figure 5 18May2015

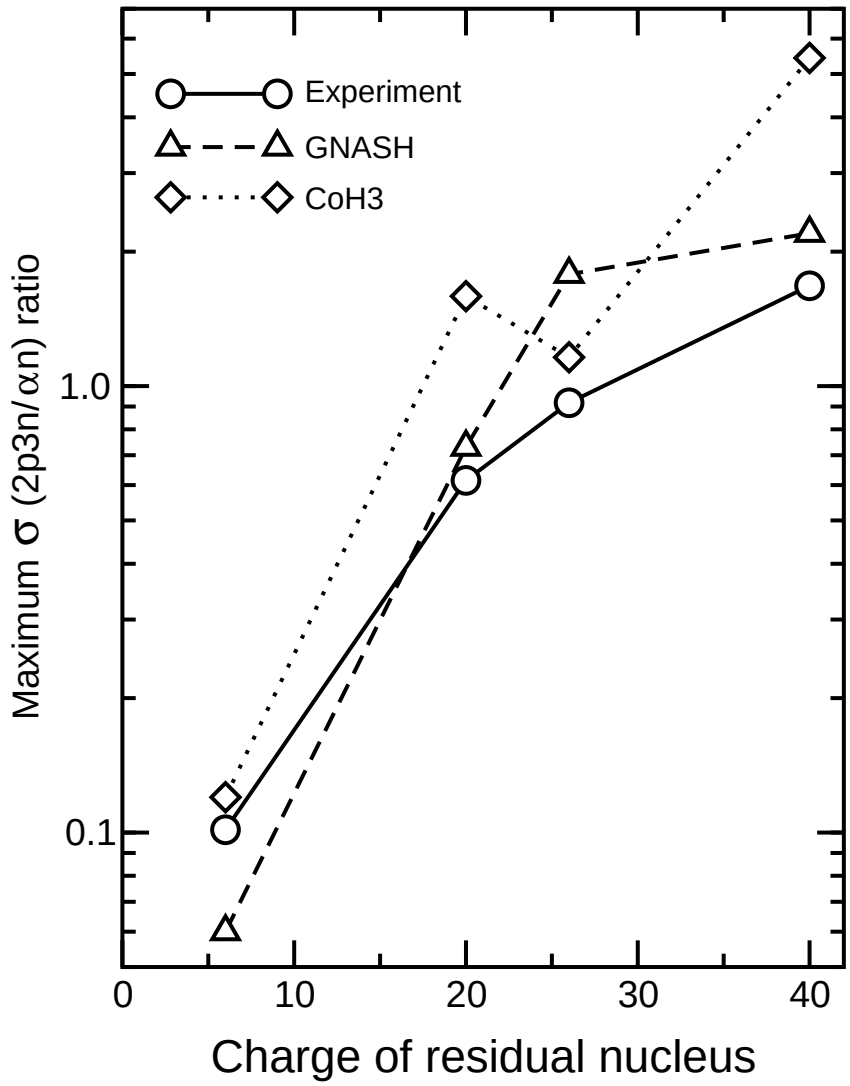

Figure 6 18May2015

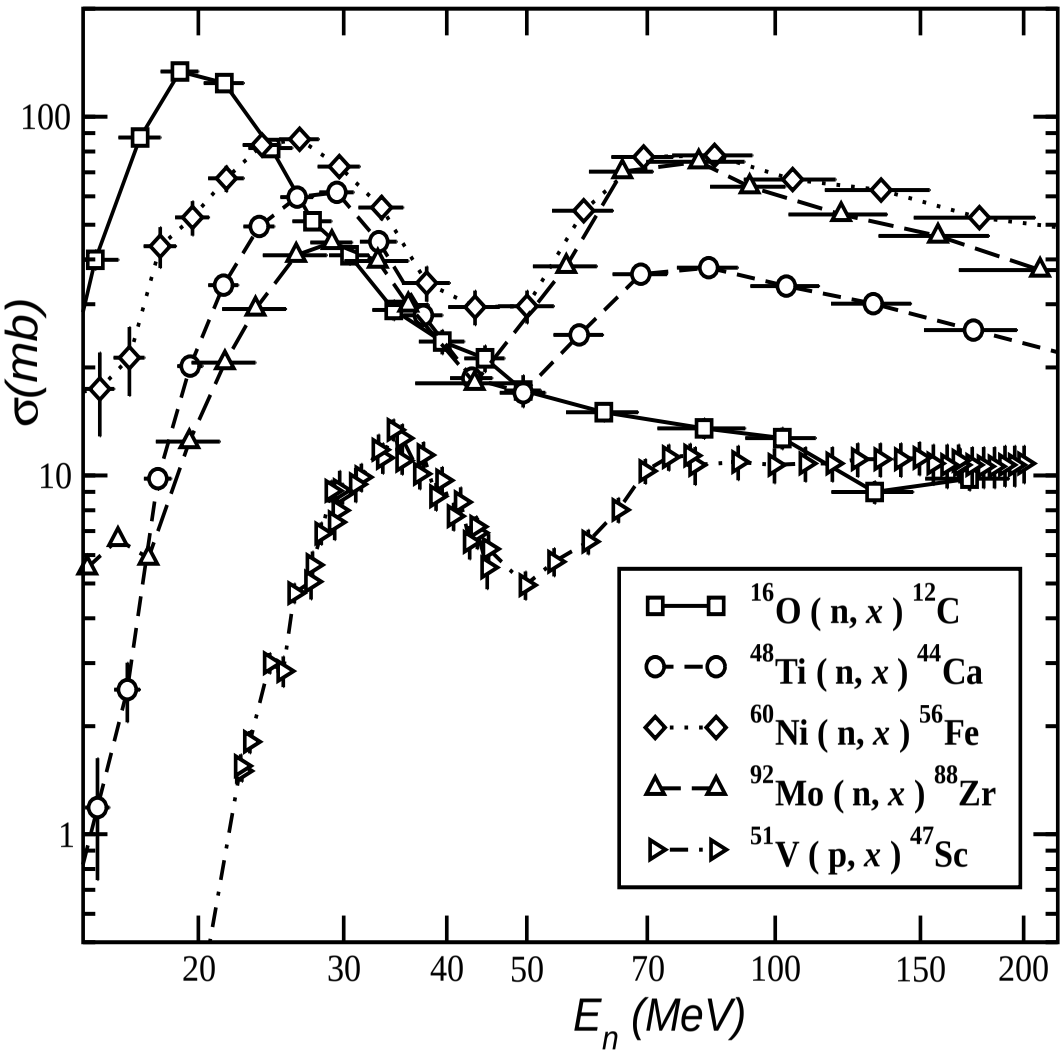

Figure 7 18May2015

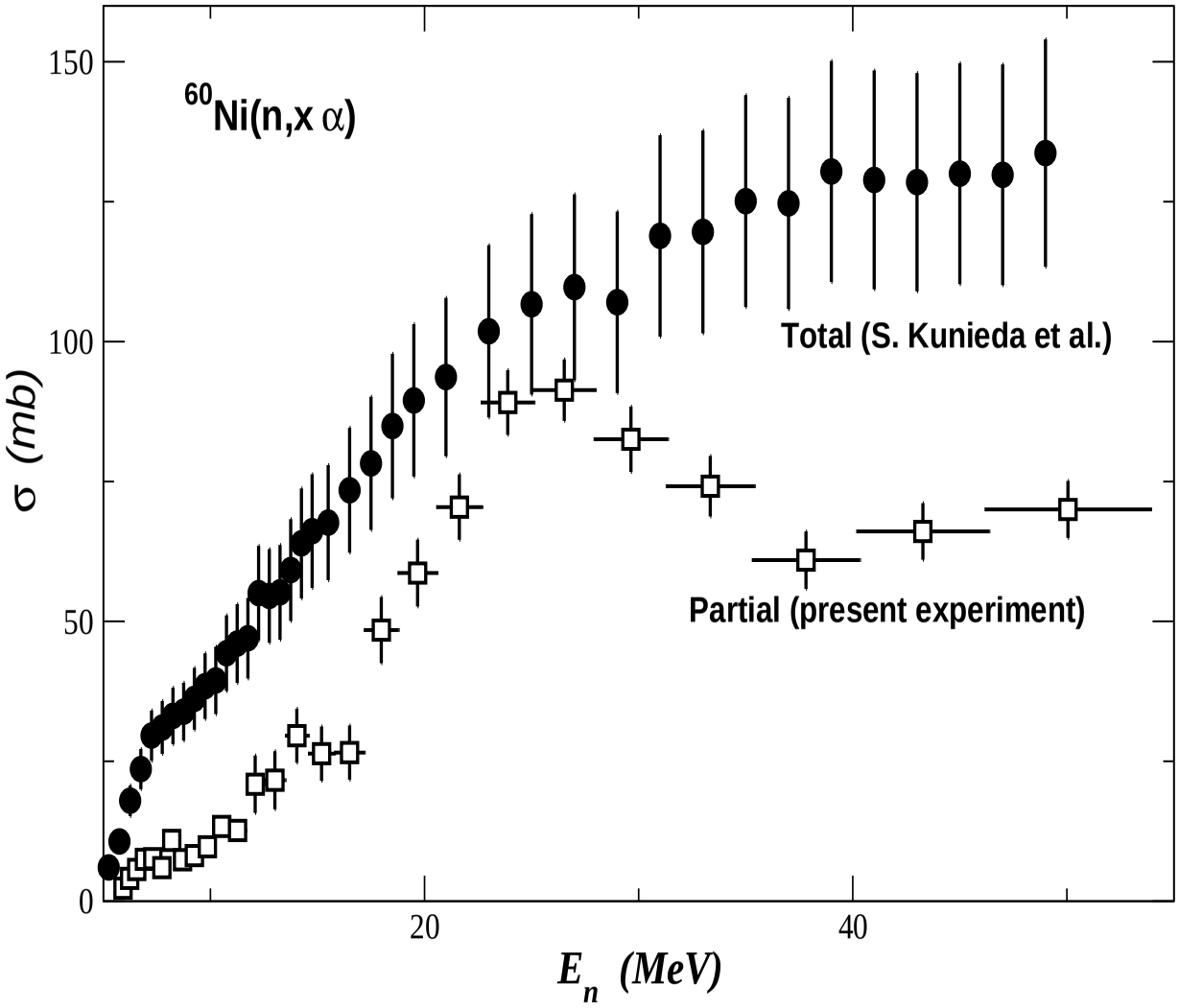

Figure 8 18May2015